X-Ray Radiography of Cryogenic Implosions on OMEGA

Introduction

Radiographs of cryogenic implosions on OMEGA[1] have been obtained using short-pulse, aluminum K-shell emission-line backlighters driven by the OMEGA EP short-pulse laser.[2] These experiments[3] have been designed to implode cryogenic D_2/DT shells and to achieve conditions that scale up to the thermonuclear ignition conditions[4] that can be attained with the much greater energy available on the NIF (National Ignition Facility).[5] X-ray radiography is being developed to verify the integrity of the imploding cryogenic shells and to corroborate the compression performance measured from charged-particle spectra.[3] The backlighter is chosen so that the emission-line energies occur where the energy-dependent optical thicknesses of the imploded cores will provide a measurable range of radiographic transmission near the time of peak compression. Backlighter simulations show that it can overcome the imploded core self-emission. The OMEGA EP short-pulse capability provides a backlight exposure time that is short enough to discern the overall shell integrity and convergence, as well as shell structure resulting from the low-order hydrodynamic effects of drive nonuniformity, target positioning offset, and ice-layer nonuniformity. Numerical simulations of the first measured cryogenic implosion radiographs[6] are used to assess the implosion performance in advance of peak compression. The radiographic simulation takes into account the spatial and temporal resolution, the camera spectral response, and the backlighter spectrum. Radial mass distributions are obtained from the radiographs using Abel inversion and the known temperature and density dependence of the free-free (FF) opacity of the hydrogen shell. This extends similar analyses of warm-shell radiographs, based on the simpler temperature and density dependence of the CH bound-free (BF) opacity, which has been applied to warm polar-drive implosions.[7] Radiography based on Compton scattering of hard backlight x rays approaching 100-keV energy[8,9] is being investigated as an alternative approach.

The measurements presented here are preliminary but are consistent with simulated implosion performance and radiography in advance of peak compression. They are valuable in planning future measurements that will be extended to the final phases of the implosion.

This article describes the experimental configurations. The atomic physics of both FF and Compton radiography, which is the basis for analyzing radiographs and for anticipating the relative advantages of each method, is described. The simulations demonstrate the feasibility of soft x-ray FF radiography and hard x-ray Compton radiography. Simulations of backlighters and radiographs are based on quantitative atomic physics and radiative transport. Finally, the available FF radiographs are analyzed, and conclusions are presented.

Experimental Configurations

The initial experimental configuration with FF radiography of cryogenic implosions includes a 10-μm-thick, 1-mm-sq Al-foil area backlighter target attached to the wire support for a silk-mounted target (Fig. 123.20). The backlighter foil is irradiated with a single 1-kJ, 10-ps OMEGA EP beam. Time-resolved backlit images are recorded through a pinhole array with an x-ray framing camera that provides 30-ps time gating.[10] The energy band, including the Al K-shell lines, is isolated using transmission filters and Ir-coated mirrors that reject hard backlighter x rays above 2 keV. One measured image is shown. The shadow of the imploding shell is visible against the emission from the irradiated spot on the backlighter foil. Further development of this diagnostic will include narrowing the camera bandwidth, possibly employing a monochromatic imaging device to further reduce the background caused by self-emission from the imploded target.

The experimental configuration for Compton radiography, shown in Fig. 123.21, is very similar to the configuration for FF backlighting.[11] The backlighter target is a 10-μm Au microwire embedded in a 300-μm-sq CH foil substrate. The 1-kJ, 10-ps OMEGA EP beam is focused onto a small 100-μm-diam spot to create a pulse of suprathermal electrons that drive a burst of K_α and bremsstrahlung emission from the microwire in a broad spectral range centered near 90 keV. By aligning the wire along the line of sight to the target, the end-on view

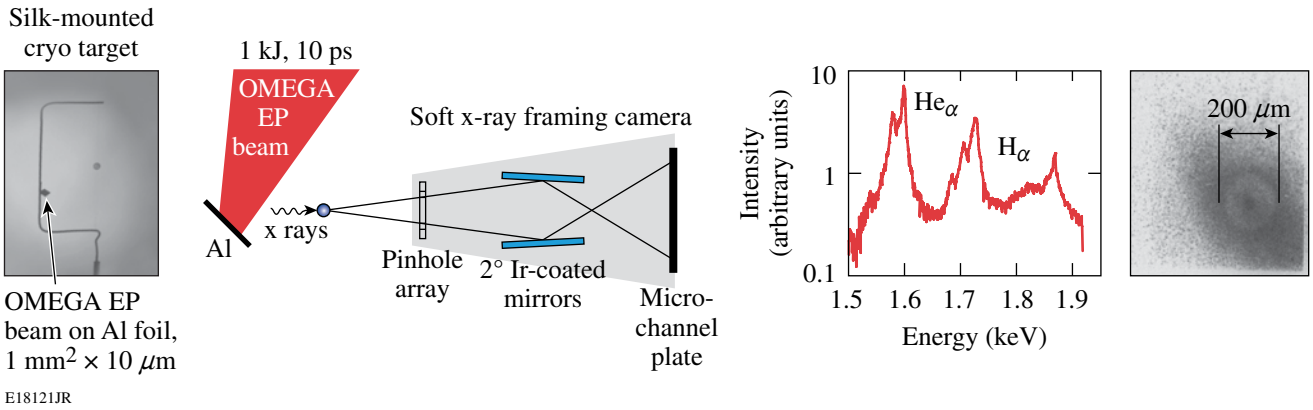

Figure 123.20
The configuration of our initial experiments with free-free (FF) radiography of cryogenic implosions includes an Al-foil area backlighter target attached to the wire support of a silk-mounted target. The backlight from the foil is driven with a single 1-kJ, 10-ps OMEGA EP beam. Time-resolved backlit images are recorded through a pinhole array with an x-ray framing camera. One measured image is shown. The shadow of the imploding shell is visible against the emission from the irradiated spot on the backlighter foil. The imaged photon energy band, including the Al K-shell lines, is isolated using transmission filters and Ir-coated mirrors.

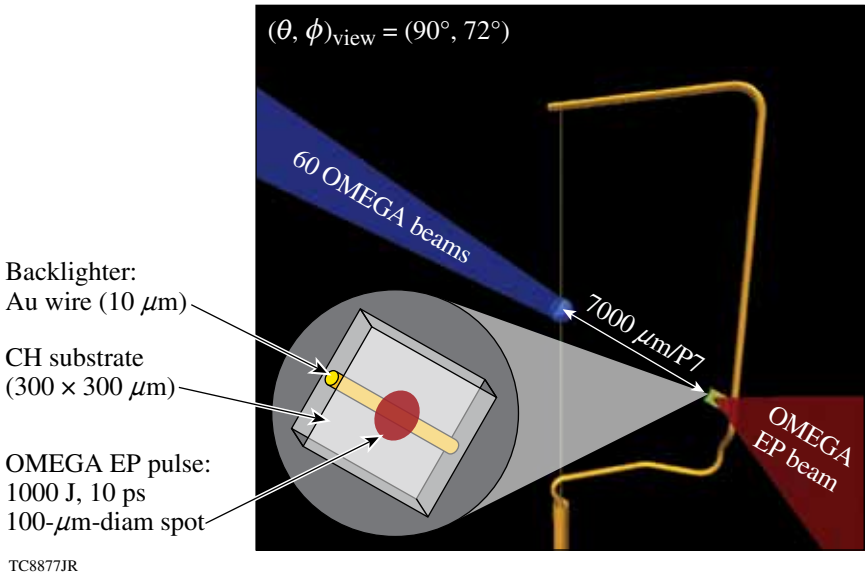

Figure 123.21
The configuration under development for Compton radiography is very similar to the configuration for FF backlighting. The backlighter target is a 10-μm Au microwire embedded in a CH-foil substrate. The 1-kJ, 10-ps OMEGA EP beam is focused to a small 100-μm-diam spot to create a burst of K_α and bremsstrahlung emission from the microwire in a broad spectral range centered near 90 keV. The end-on view of this wire appears to the image plate as a point backlighter.

of this wire appears from the direction of the image plate as a point backlighter. Preliminary radiographs of warm CH target implosions have been obtained with this configuration on OMEGA by Tommasini.[9] This method is currently being applied to cryogenic implosions.

Atomic Physics Basis for Radiography

A radiograph is formed by the attenuation of backlighter emission by an object, creating a shadow of the object in an imaging device. This process is illustrated in Fig. 123.22 for a spherical object creating a circularly symmetric shadow. The image intensity $I(x)$ is a central lineout of the measured intensity distribution along the x axis of the image plane coordinates x,y with y fixed accordingly. All the backlighter rays, propagating in parallel, create an orthographic projection of the object on the image plane, as if the backlighter were infinitely far away. The intensity $I(x)$ is the attenuated backlighter intensity I_{BL}. The attenuation is given by $I(x) = I_{BL} \exp[-\tau(x)]$, where $\tau(x)$, the optical thickness of the object along a particular line of sight from the backlighter to the point x on the image plane, is the path integral $\tau(x) = \int \kappa(s)\,ds$ of the opacity of the object $\kappa(s)$, expressed as a function of position along the path, indicated by the path-length parameter s (Ref. 12). If the opacity of the object is a known function of its conditions, an optical thickness measurement will provide a diagnostic of conditions along the line of sight. Writing $\kappa[r(s)]$ in Fig. 123.22 shows that the points on the path s correspond to points r in a spherical opacity distribution and that the two are related in a well-defined way. This relationship forms the basis for inferring $\kappa(r)$ from $\tau(x)$ by Abel inversion,[13] as described below.

The FF, bound-free (BF), and Compton radiography techniques are distinguished by the properties of the respective dominant absorption or scattering processes involved. The FF and BF processes have strong material dependence and share the same ν^{-3} spectral dependence, while the effective radiographic mass absorption coefficient of Compton scattering is only weakly dependent on material composition and the backlighter spectrum. Figure 123.23 shows these three individual contributions [FF (red), BF (blue), Compton (black)] plotted for deuterium (solid lines) at a typical coasting-phase shell condition, ρ = 3 g/cm^3 and kT = 25 eV, and for carbon (dashed lines) at ρ = 0.5 g/cm^3 and at a higher temperature, kT = 100 eV, where it might exist in trace concentrations at the outer edge of the imploding shell, near a cooling remnant of the hot ablation region. Blue ovals indicate the key process and typical spectral range for FF radiography of cryogenic D_2 shells, BF radiography of warm CH shells, and Compton radiography of most materials. For the purpose of radiography, it is acceptable to think of opacity or attenuation being caused by Compton scattering, even though Compton scattering is not an absorption process in which photons are destroyed. At the photon energies being considered, the scattering is only about 30% stronger in the forward direction than the backward direction.[14] This is sufficiently isotropic that nearly every scattered photon is effectively removed from the field of view, as if it has

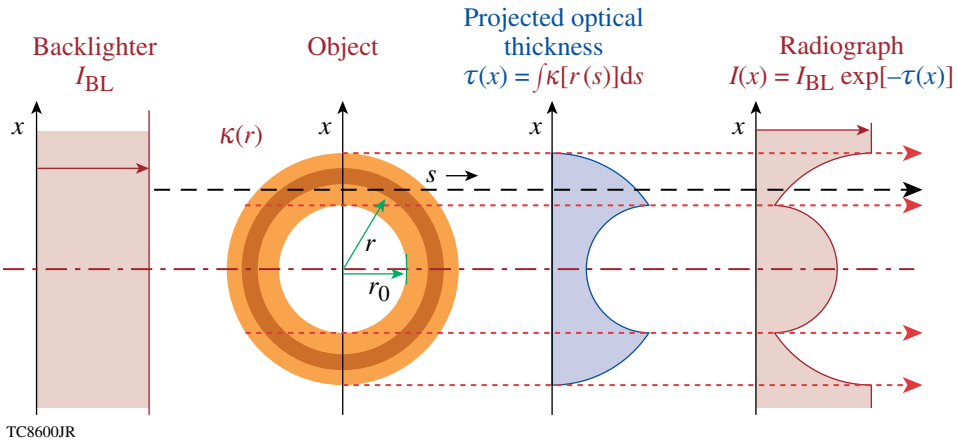

Figure 123.22
Hollow shells with radial opacity profiles $\kappa(r)$ form characteristically limb-darkened circularly symmetric shadows in the image plane, here represented as $I(x)$. A typical backlighter emission ray is shown sampling the absorbing shell on its way to the image plane, where the recorded intensity is determined by the integral of the opacity along its path, the projected optical thickness. Abel inversion recovers the radial opacity distribution from the optical depth profile projected onto the image plane.

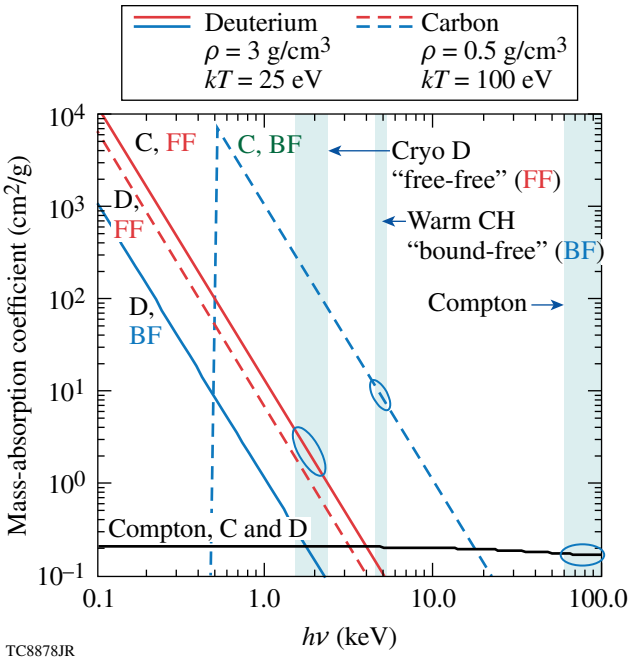

Figure 123.23
The FF, BF, and Compton radiographies are distinguished by the properties of the respective attenuation processes involved. FF and BF mass-absorption coefficients have strong material and spectral dependence, while the effective mass-absorption coefficient of Compton scattering is only weakly dependent on material composition and the backlighter spectrum. The individual process [FF (red), BF (blue), Compton (black)] contributions are plotted for carbon (dashed lines) and deuterium (solid lines) at a typical set of coasting-phase conditions for an imploding deuterium shell. Blue ovals indicate the key process and spectral region for FF radiography of cryogenic deuterium shells, BF radiography of warm CH shells, and Compton radiography of most materials.

been absorbed, so the total Compton-scattering cross section for radiography may be treated as an absorption cross section.

Target optical thicknesses of order unity are desirable for radiography. As a typical OMEGA target implosion approaches peak compression, the mass areal density of a shell grows by more than an order of magnitude within roughly 100 ps, peaking at roughly 0.3 g/cm^2 (Ref. 3). Based on this, the mass-absorption coefficients in the neighborhood of 10 cm^2/g are appropriate. For BF and FF radiography, which share the same strong ν^{-3} spectral dependence, this determines the appropriate range of backlighter energy. The Compton cross section, on the other hand, given by the Klein–Nishina formula, varies very slowly with photon energy out to 100 keV (Ref. 15), the upper limit of hard x-ray backlighters proposed thus far.[8] This makes Compton scattering the dominant radiography process for light elements at high-photon energies. The advantage of radiography with hard x rays is that the self-emission of the imploded target, which decreases rapidly with photon energy as exp(–$h\nu$/kT), does not create significant background intensity at these high backlighter photon energies. The main disadvantage of Compton radiography is that the attenuation by OMEGA-imploded shells is small, of the order of several percent at peak compression. An advantage of Compton scattering is that its very weak spectral dependence simplifies the analysis of Compton radiographs. With broadband BF and FF radiography, the spectral content of the backlighter and the spectral response of the imaging system must be known accurately because of the strong spectral dependence of BF and FF opacity. The weak spectral dependence of Compton scattering is also a disadvantage because one cannot adjust the backlighter energy to obtain anything more favorable than weak attenuation. Compton radiography will be better suited to the NIF,[5] where implosions approaching the 3.0-g/cm^2 mass areal density required for ignition[16] will provide optical thicknesses an order of magnitude larger than on OMEGA.

The mass-absorption-coefficient curves for Compton scattering by carbon and deuterium are indistinguishable, so they are represented by the same black curve in Fig. 123.23. For hard x rays, all electrons, free and bound, contribute identically to the mass-absorption coefficient.[15] Since most of the naturally occurring elements from helium through chlorine have equal proton and neutron numbers, they have very nearly the same number of electrons per mass and, therefore, very nearly equal Compton mass-absorption coefficients. The mass-absorption coefficient of heavier elements decreases slowly with atomic number, as the proton/neutron number ratio decreases. Under compressed-shell conditions beyond the late coasting phase, carbon is more opaque than hydrogen by a few orders of magnitude, due, in large part, to the strong atomic-number Z^4 scaling of the K-shell photoionization cross section and the dominant abundance of helium-like carbon, with two bound K-shell electrons per ion. Hydrogen, on the other hand, has a negligible population of bound states under these conditions and, as a result, absorbs primarily through FF absorption. This means that a trace of carbon impurity in an imploding hydrogen shell will dominate its radiograph. If the purpose of the radiograph is to observe the mass distribution, then a hydrodynamically irrelevant trace of carbon contaminant can substantially alter the apparent mass distribution in a FF radiograph of an imploding cryogenic shell, while Compton radiographs will remain largely unaffected. If the purpose of the radiograph is to detect carbon contamination by fuel–shell mix, it will be visible through its high BF opacity at the soft

energies of FF radiography and invisible at the hard energies of Compton radiography.

In the case of radiography of CD shells,[7] the opacity is dominated by the BF opacity of the helium-like species of carbon over the wide range of temperature and density expected in imploding shells. The remaining dependencies are $\rho\nu^{-3}$. Assuming that the backlighter spectrum and the detector response define a single effective photon energy, the opacity becomes simply a product of the mass density ρ and a known constant factor. Consequently, each optical thickness measurement is equivalent to a measurement of $\int \rho \mathrm{d}s$, the areal density along a particular line of sight. The analysis of D_2 shell FF radiographs is simplified by the fact that ionization under imploded shell conditions is likely to be sufficiently complete that BF transitions will not compete with the FF opacity. The remaining parameter dependencies are $\rho^2 T^{-1/2}\nu^{-3}$, so each optical thickness measurement in a FF radiograph at a known ν is equivalent to a $\int \rho^2 T^{-1/2} \mathrm{d}s$ measurement. Given an independent determination of the temperature T, such as from another diagnostic or from a simulation, the integral $\int \rho^2 \mathrm{d}s$ remains. The radial density–squared profile can be obtained from this data by Abel inversion, just as has been done with CD shells.[7] The uncertainty of the density inferred from FF opacity is correlated with the uncertainty in the temperature, but only weakly, since the temperature scaling of FF opacity is $T^{-1/4}$, relative to the density dependence.

The opacities of both CD and D_2 follow these simple temperature and density-scaling laws over much of the range of conditions of compressed imploded shells. This is shown in Fig. 123.24 in two plots of their respective temperature-and-density–scaled opacities as functions of temperature. The photon energy is fixed at $h\nu = 2$ keV, and the scaled opacity is plotted for four different densities roughly a factor of 10 apart. In Fig. 123.24(a), the plotted quantity is equal to the opacity divided by ρ, corresponding to the scaling of BF absorption, which dominates the opacity of CD; Fig. 123.24(b) shows the opacity of D_2 divided by $\rho^2/T^{1/2}$, corresponding to the scaling of FF absorption, which dominates the opacity of D_2 under these conditions. The nearly constant value over a wide range of temperature indicates the validity of the respective temperature and density scalings. The CD opacity drops from this scaling at temperatures above 100 eV because the bound electrons are removed by collisional ionization and rises above this scaling at the highest density because of the contribution of FF absorption that grows with density as ρ^2. The simple scaling of the FF opacity of D_2 is seen to hold for all the conditions plotted, except for the lowest density, where bound electron

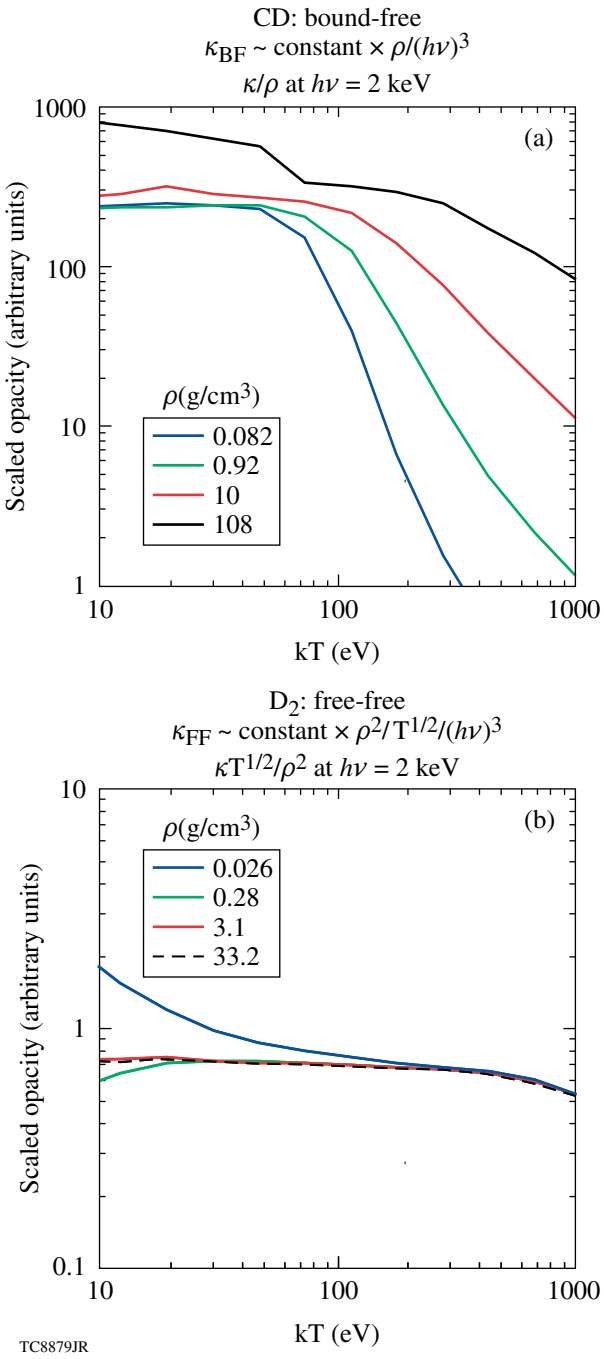

Figure 123.24
The opacities of CD and D_2 both follow simple temperature- and density-scaling laws that cover much of the range of conditions of compressed imploded shells. This is shown in two plots of their respective scaled opacities as functions of temperature. Plot (a) shows the opacity divided by ρ, corresponding to the scaling of BF absorption, which dominates the opacity of CD. Plot (b) shows the opacity of D_2 divided by $\rho^2/T^{1/2}$, corresponding to the scaling of FF absorption, which dominates the opacity of D_2 under these conditions. The scaled opacities are plotted for four different densities at roughly a factor of 10 apart. The photon energy is fixed at $h\nu = 2$ keV.

states become marginally abundant at the lowest temperatures. The scaling of the FF opacity is not as simple as that of BF opacity, but it appears to be slightly more reliable, at least over the conditions and spectral range shown.

Ideally, the backlighter should be monochromatic so that ν is a known constant. If the opacity of the object varies significantly over the joint bandwidth defined by the backlighter spectrum and the detector response, it can significantly alter the transmitted backlighter spectrum. Therefore, however one might define a spectrum-averaged backlighter energy, its value may vary over the plane of the radiograph. This almost certainly will not be an issue with Compton radiography since the effective opacity, as shown in Fig. 123.23, varies very slowly with photon energy. In any case, the main benefit of a narrow-bandwidth detector is that it limits the background caused by self-emission from the target.

Feasibility of Soft X-Ray Free-Free Radiography

The simulation of cryogenic implosion radiography employs several tools. The target implosions are simulated in 1-D by *LILAC*[17] and in 2-D by *DRACO*,[18] which includes the effects of target offset and irradiation nonuniformity (see "Two-Dimensional Simulations of the Neutron Yield in Cryogenic-DT Implosions on OMEGA," p. 111). The short-pulse foil hydrodynamics are simulated in 1-D by *LILAC*. Both the backlight emission and the implosion radiography are simulated separately by the post-processor Spect3D.[19] Spect3D calculates radiation transport using tabulated opacity and emissivity data based on detailed atomic models for the radiograph simulations. For the backlighter simulations, these quantities are calculated in real time, using time-dependent, non-LTE atomic-level kinetics, including self-consistent nonlocal photoexcitation.

The radiographs are simulated from the opacity distributions within the object that are obtained from hydrodynamic simulations. The calculation takes into account the spectral, spatial, and temporal responses of the imaging device as well as the backlighter spectrum. This fully accounts for the finite-bandwidth effect discussed above.

Figure 123.25 shows a *DRACO*/Spect3D-simulated radiograph of a successful OMEGA cryogenic implosion. This implosion, shot 47206, reached a measured areal density of 202±7 mg/cm^2 (Ref. 20). The radiograph, which is shown in (b), shows the shadow of the simulated mass-density profile at the time of peak compression, which is shown in (a). This contour plot is a cross section of the density distribution in a plane intersecting the imploded shell along its vertical symme-

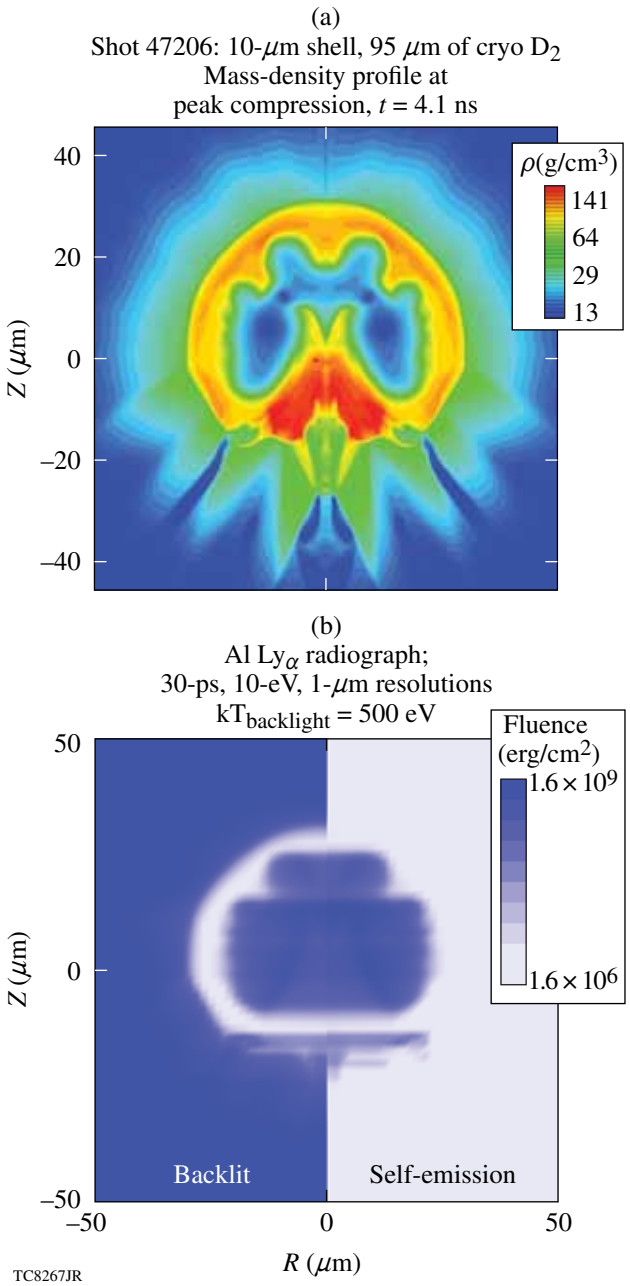

Figure 123.25
A *DRACO*/Spect3D-simulated radiograph of a successful OMEGA cryogenic implosion at peak compression is shown in the left "backlit" half of the split frame in (b). This implosion, shot 47206, reached a measured areal density of 202 mg/cm^2 (Ref. 20). The simulated mass density profile at this time is shown in cross section in the contour plot in (a). The coordinates (R,Z) refer to a cylindrical geometry with the symmetry (Z) axis in the vertical direction. The simulated radiograph in the left side of the split image in (b) was backlit at the H-like aluminum Ly$_\alpha$ emission line energy at a brightness temperature of 500 eV. The right half of the split image in (b) shows only the self-emission with no backlighter contribution. The imaging device is restricted to a 10-eV bandwidth, a 30-ps integration time, and a 1-μm spatial resolution.

try axis. The asymmetries of the imploded shell are the result of irradiation nonuniformity caused by target offset, beam imbalance, and the shape of the individual beam profile at the target surface. The cylindrical coordinates (R,Z) are defined with the symmetry (Z) axis in the vertical direction. The left-hand side of the split image in (b) shows the simulated radiograph of this density distribution, including the backlighter. The right-hand half of the image is the exact mirror image of the radiograph in (a), except that the backlighter contribution is not included, leaving only the self-emission. The imaging device is restricted to a bandwidth of 10 eV. The backlighter is assumed to be the Ly_α emission line of H-like aluminum at a brightness temperature of 500 eV, which corresponds to an intensity of about twice that of the shell's self-emission at this line energy, which peaks at about this time. This intensity has been exceeded in backlighter development experiments,[21] but it has been chosen here to illustrate the useful information available with a backlighter that does not overwhelm the self-emission. The 30-ps integration time, which is comparable to currently available gating times, takes into account the blurring effects of source motion. The 1-μm spatial resolution of the simulation is much better than will be available with current instrumentation, but it shows the amount of information that could be available with improved resolution.

Most of the structure seen in the shell mass distribution is visible in the radiograph [Fig. 123.25(b)]. At the bottom of the shell, the flow appears to have formed a dense concentration of mass that has preceded the rest of the shell toward the center. The shadow of such a dense concentration of shell material should be seen distinctly in the backlit portion of the image on the left-hand side of the frame, but it is very faint. Seeing how similar this cone-shaped concentration appears in the backlit side of the frame and in the self-emission side, one concludes that it is filling in its own shadow with its own emission. The inner-surface emission from the shell behind it is being blocked along with the backlighter. The falling radial temperature gradient and the rising radial density gradient create a surface of maximum emissivity at the interior of the shell. As has been shown with BF radiographs of warm polar-drive implosions,[7] the portion of the shell outside this emitting surface forms a shadow on the radiograph that may be analyzed. As long as this shell absorption is physically separated in the radiograph from the inner-surface self-emission, it can be measured. As this example demonstrates, however, self-emission is capable of hiding substantial amounts of shell mass.

Over the 30-ps integration time, the self-emission is dimmer than the hypothetical backlight but strong enough to reduce confidence in the absorption of the shadow of the shell limb. The shape of the shell is still apparent with this marginally intense hypothetical backlighter. Higher backlight intensity will be available that will compensate for the excess self-emission admitted by gating times that are longer than the backlight pulse and by spectral pass bands that extend past the spectral width of the backlighter.

The image contrast in a FF radiograph of an imploding cryogenic shell can change from nothing to saturation in a very short time because of the rapid approach to peak shell density, coupled with the strong ρ^2 density scaling of the FF opacity. The spectrum of the backlighter must be chosen so that the shell transmission produces optimum radiographic contrast at a chosen time. The contour plot in Fig. 123.26 shows the transmission of a ray passing through the center of the *DRACO* simulation shown in Fig. 123.25 as a function of time and backlighter photon energy. This plot is repeated, once with the Al K-shell line energies indicated and once with the energies of the H-like Ly_α lines of several possible backlighter materials indicated. At any one of these line energies, the lineout across the plot gives the transmission as a function of time. This transmission varies dramatically, reaching a minimum at maximum compression near 4.15 ns. For a particular backlighter energy, Fig. 123.26 shows the times at which a desired transmission value is likely to occur. Similarly, the contour corresponding to a desired transmission value gives, as a function of time, the backlighter photon energy that would provide this transmission value. If, for example, the contour at the transition from yellow to orange indicates a suitable transmission value, it crosses the aluminum K-shell line energies roughly 100 ps before peak compression, indicating that these lines are suitable backlight sources at this time. Materials with higher line energies will provide the same degree of contrast later in time.

Figure 123.27 shows the expected performance of an Al backlighter. The time-resolved spectrum in (a) represents the simulated spectral flux from a 10-μm aluminum foil irradiated with an 8-ps Gaussian pulse at 10^{18} W/cm^2. The strongest feature is the Ly_α emission line of the hydrogen-like species, but a great deal of energy is emitted in other spectral features, including continuum above 2.2 keV. This continuum would create a uniform background, were it not removed by iridium reflectors, as was explained earlier and shown in Fig. 123.20. The specific intensity at the Ly_α line center is shown in (b) as a function of time. This emission appears as a pulse lasting 5 ps, centered close to the laser pulse. The specific intensity of this emission line can be compared with that of the time-dependent self-emission expected from a cryogenic implosion

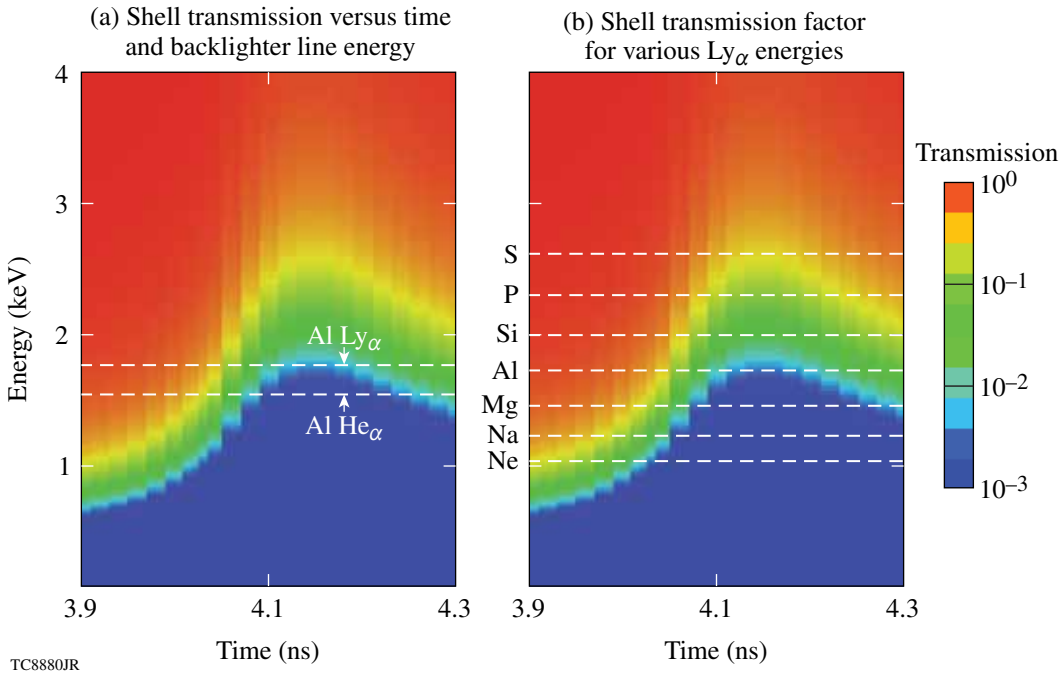

Figure 123.26
The image contrast in a FF radiograph is determined by the transmission of the imploded shell at the effective photon energy of the backlighter. The transmission of a ray at the center of a *DRACO*-simulated radiograph of shot 47206 is shown plotted as contours as a function of time and backlighter photon energy. This plot is repeated, once with the Al K-shell line energies indicated and once with the energies of the H-like Ly$_\alpha$ lines of several possible backlighter materials indicated. The backlighter energy giving a particular transmission value at a particular time can be read as a function of time by following the corresponding contour.

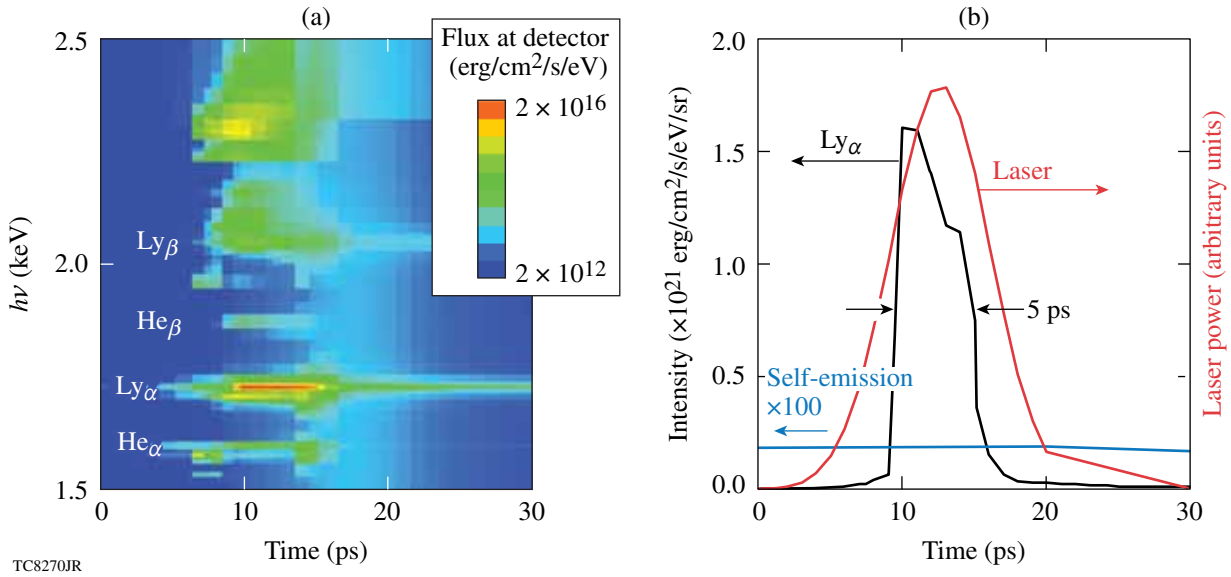

Figure 123.27
The simulated time-resolved spectrum in (a) represents the spectral flux from the surface of a 10-μm aluminum foil irradiated with an 8-ps Gaussian pulse at 10^{18} W/cm^2. The specific intensity centered at the Ly$_\alpha$ line is shown in (b) plotted as a function of time. This emission appears as a pulse lasting 5 ps, centered near that of the laser pulse, plotted in red. This emission line is much more intense than the self-emission expected from a cryogenic implosion on OMEGA. The blue curve represents 100× the specific intensity obtained from an implosion simulation, assuming that all the self-emission of a simulated imploded cryogenic core emerges from within a 20-μm-radius circle.

on OMEGA. The time scale of the simulated implosion has been shifted so that the peaks of the self-emission and the backlight line intensity coincide. The blue curve represents 100× the specific intensity obtained assuming that the entire self-emission of a simulated imploded cryogenic core emerges from within a 20-μm-radius circle. Clearly, the Ly$_\alpha$ line can provide a backlight source that is potentially two orders of magnitude more intense than the self-emission background. The self-emitted continuum lasts much longer, however, than the short duration of the backlighter and covers a much wider bandwidth than the backlighter spectral line, so short framing times and narrow bandwidths are essential for restricting the self-emission background to acceptable levels.

The simulated spectral fluence is compared in Fig. 123.28 with the measured time-integrated spectral emission from a similar experiment on the OMEGA EP laser. The consistency of the simulated and measured aluminum Ly$_\alpha$ fluence is encouraging. The irradiance of 1.25×10^{18} W/cm^2 in the simulation is slightly higher than the 5×10^{17} W/cm^2 average in the experiment, which anticipates the likelihood that more-intense portions of the nonuniform beam are dominating the spectral emission. To convert the measured fluence to a time-integrated specific intensity that can be compared directly with the simulated time-integrated emission, it is assumed that the measured fluence was emitted within a length of time equal to the backlighter laser pulse width and from within its nominal 23-μm laser-spot radius. With these assumptions, the simulated and measured Ly$_\alpha$ fluences are close. The measured He$_\alpha$ fluence, on the other hand, is much higher than the simulated level. The measured background continuum is also much higher than the simulated level. These discrepancies are probably due to emission from the foil outside the directly illuminated spot that has been heated by both thermal and nonthermal electron transport. The formation of a large, relatively cool radiating area surrounding the laser spot, following the absorption within the laser spot, has not been taken into account in the 1-D *LILAC* simulation. Even though the colder radiating area would be dimmer than the original hot area under the laser, it could be larger and longer lasting, resulting in a substantial contribution to the total fluence. The agreement in the Ly$_\alpha$ emission indicates that the prompt emission from the laser spot is modeled reasonably well. The He$_\alpha$ emission certainly comes from a lower temperature and a larger area than the Ly$_\alpha$ source because material producing more He$_\alpha$ emission than Ly$_\alpha$ emission can have a temperature of no more than about 500 eV. At this temperature, the blackbody limit on the line emission rules out the possibility that such a source could produce the observed He$_\alpha$ fluence in a time as short as the laser pulse width and from an area as small as the laser-spot area. If the Ly$_\alpha$ emission is prompt and the He$_\alpha$ emission is over an extended period of time, then it is the Ly$_\alpha$ emission that will be favored by the time gating of the x-ray framing camera. Given the ν^{-3} dependence of the FF opacity of the imploded shell, uncertainty as to which of these two spectral lines is dominating the backlighter over the gating time corresponds to less than a 24% uncertainty in the shell opacity to be used in the radiographic analysis. With reasonable progress in backlighter spectroscopy or by implementing narrow-band imaging, this uncertainty will diminish substantially.

For comparison, the time-integrated self-emission intensity from the previous simulated cryogenic implosion example is plotted as the blue curve in Fig. 123.28, assuming for the purposes of this estimate that the source is a disk with a 20-μm radius, which is very close to the image size at peak core emission. This self-emission is much lower than the Ly$_\alpha$ spectral fluence, indicating that the implosion radiographs can be substantially free of self-emission, with some tolerance of longer

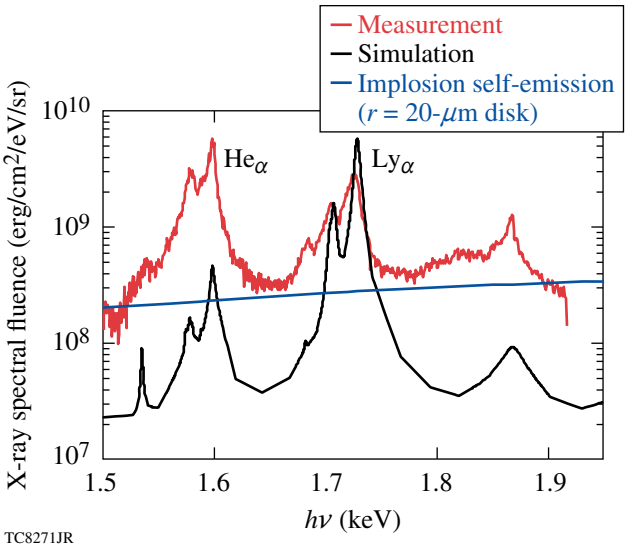

Figure 123.28
The measured and simulated spectral fluence from an aluminum foil target are compared, assuming identical pulse widths and similar irradiances and assuming that all emission comes from within a 23-μm laser spot. The simulated aluminum Ly$_\alpha$ time-integrated spectral fluence is consistent with the measured spectral emission. Agreement over the entire spectrum cannot be expected from a 1-D simulation like this because nonthermal electron transport to non-irradiated portions of the foil is not modeled. Agreement in the Ly$_\alpha$ fluence indicates that emission from the directly irradiated spot is modeled reasonably well and that useful backlighter intensities can be attained. The time-integrated intensity from a simulated cryogenic implosion is plotted for comparison, assuming that the effective source is a 20-μm-radius disk, which is very close to the core image size at peak core emission.

integration times and camera bandwidths that are slightly wider than the backlighter spectral line.

DRACO/Spect3D-simulated radiographs of the cryo implosion shown in Fig. 123.25, shot 47206, have been obtained using the simulated backlighter spectrum shown in Fig. 123.27. Three images, representing the 100 ps leading up to the time of peak compression, are shown in Fig. 123.29. The spectral interval used is 10 eV in width, centered at the aluminum Ly$_\alpha$ energy. These radiographs show a very rapid increase in image contrast, roughly an order of magnitude in each 50-ps time step. At this backlighter energy, the 100 ps shown is the extent of the useful time interval for radiography with Al lines, because of the loss of contrast at the early end of this interval. As explained above, the degree of radiographic contrast obtained at a given time in the implosion can be adjusted by changing the backlighter material. The simulated backlighter intensity is high enough in these radiographs to overcome the self-emission. The image at 4.1 ns shows the shadow of the mass concentration at the bottom of the imploded shell, which was not visible in the simulated radiograph in Fig. 123.25, obtained with marginally adequate backlighter intensity. The simulated spatial resolution of 5 μm allows one to see much of the detail of the mass distribution in Fig. 123.25. The assumed temporal resolution is 30 ps and the shell motion is taken into account. The effects of the assumed spatial resolution of 5 μm and the smearing resulting from shell motion during the 30-ps time gate are comparable.

Feasibility of Hard X-Ray Compton Radiography

Simulated Compton radiographs are obtained from *DRACO* and *LILAC* simulations using the same Spect3D postprocessor as the simulated FF radiographs. The effective opacity is much simpler. Along any line of sight, the density path integral $\int \rho ds$, and the effective optical depth τ are very simply related by

$$\tau = \frac{\sigma_{KN}(h\nu)}{m_{Z,A}/Z} \int \rho ds, \tag{1}$$

where $\sigma_{KN}(h\nu)$ is the Klein–Nishina total cross section for the Compton scattering of a photon.[14,15] This cross section varies very slowly over the 50- to 100-keV spectral range used for Compton radiography, and, at these energies, all electrons in the material, both bound and free, contribute equally to the effective opacity. Consequently, the areal electron density is obtained from the areal mass density by dividing by $m_{Z,A}/Z$, the mass per electron of the shell material, specified here by its atomic number Z and mass A. Since the mass per electron is about two atomic mass units, decreasing slowly with increasing atomic number, the effective opacity has a very weak material dependence.

The three *DRACO*/Spect3D-simulated radiographs of shot 47206 in Fig. 123.29 are calculated again and shown in Fig. 123.30 at the same times and spatial resolutions, but with

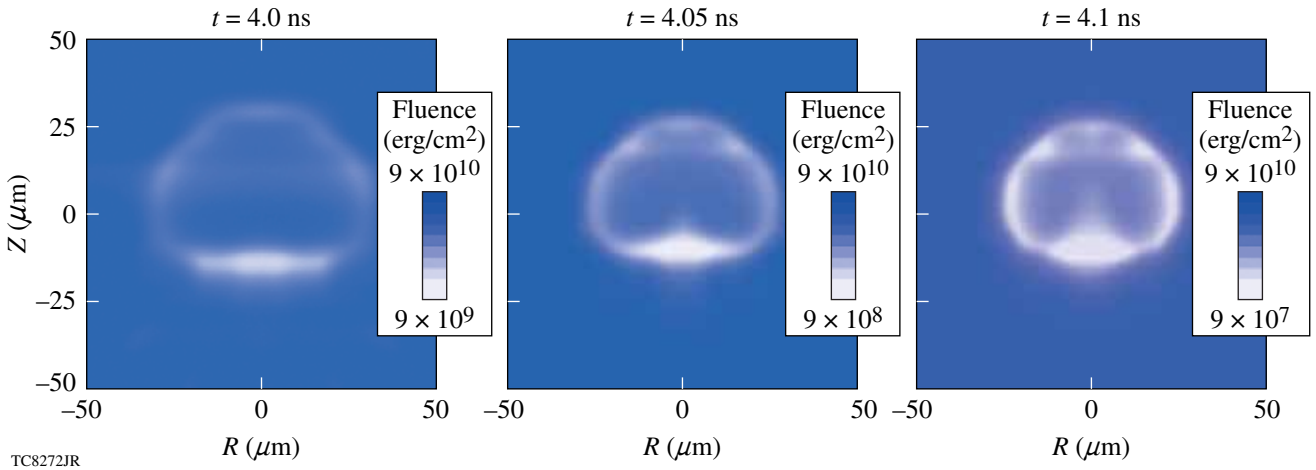

Figure 123.29
Three simulated FF radiographs leading up to the time of peak compression are shown, based on the same simulation shown in part in Fig. 123.25 and the backlighter spectrum shown in Fig. 123.28. The spectral interval used is 10 eV in width, centered at the aluminum Ly$_\alpha$ energy. The assumed spatial resolution is 5 μm and the temporal resolution is 30 ps. These images illustrate that useful detail is visible and also that radiographic contrast increases very rapidly as peak compression is approached.

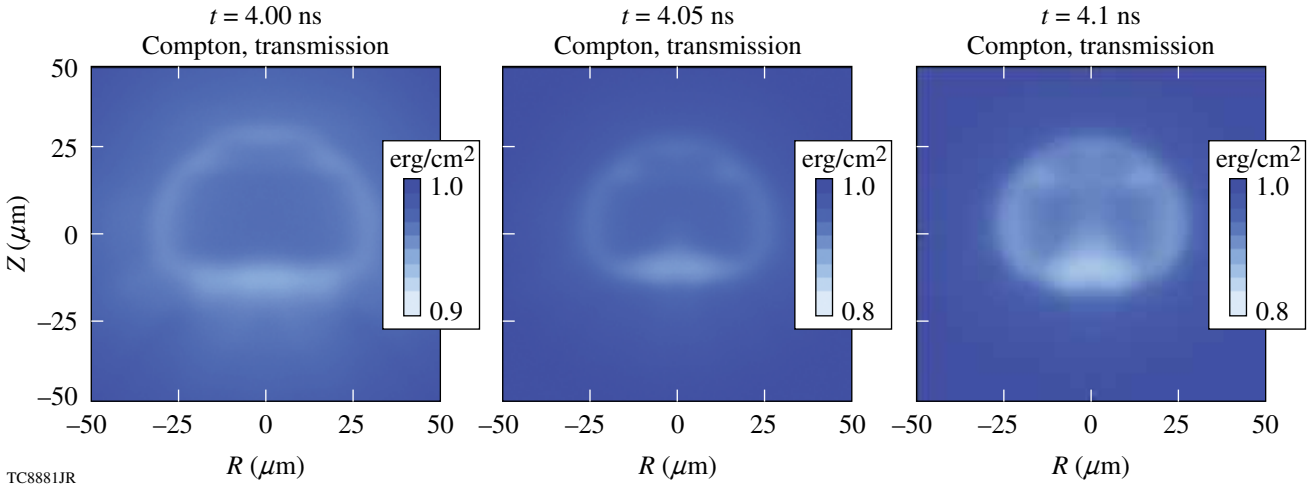

Figure 123.30
The three *DRACO*/Spect3D-simulated radiographs of shot 47206 in Fig. 123.29 have been obtained at the same times and spatial resolutions but with a backlighter energy of 57 keV, where Compton scattering forms the image. The time resolution is 10 ps, the pulse width claimed for recent Compton radiograph experiments with warm CH shells. The Compton radiographs appear almost identical to the FF radiographs, except for their very weak transmission signal.

a backlighter energy of 57 keV, where Compton scattering forms the image. The time resolution is 10 ps, the pulse width claimed for recent Compton radiograph experiments with warm CH shells.[9] The Compton radiographs appear almost identical to the FF radiographs, except for their very weak transmission signal. The contour scales are linear and cover only the range of transmission needed to bring out the image, while the FF radiographic images in Fig. 123.29 require logarithmic scales covering up to three decades to span their full dynamic range. The backlighter photon energy of 57 keV corresponds to the inner-shell K_α decay transition of tantalum. Since this simulation was done, higher energy sources have been considered, including bremsstrahlung up to 100 keV (Ref. 8), but the result of this simulation would change negligibly if this were taken into account, owing to the weak energy dependence of the Klein–Nishina cross section.

A *LILAC*/Spect3D simulation of a sequence of Compton radiographs has been obtained for the 120 ps leading up to the time of peak compression of a more-recent cryogenic implosion, shot 55723. The simulated peak areal density was 370 mg/cm^2, and the measured value was 300 mg/cm^2 (Ref. 3). The simulated shell areal density and neutron emission rate are plotted as functions of time in Fig. 123.31(a). The simulated radiographs are circularly symmetric because the *LILAC* simulation is spherically symmetric, so the simulated radiographs are represented as radial transmission profiles in Fig. 123.31(b). The transmission profile curves are color keyed to a legend giving the image times and also to time markers in (a). This shows that the imaging device must be sensitive to a 15% attenuation signal. A much greater sensitivity will be required for quantitative radiography at earlier times. Sensitivity to less than 4% attenuation will be needed to make measurements 120 ps before peak compression. This series of radiographs shows that both the radial convergence and the transmission are measurable indicators of compression. The core shadow shrinks and sharpens with the approach to peak compression, but the opaque limb of the image converges by only 10 μm over the 120 ps shown, making this motion difficult to measure, given the 10-μm image resolution imposed by the size of the point backlighter. These radiographs were simulated without allowance for temporal or spatial resolution.

Analysis of Free-Free Radiographs

The FF radiographs obtained thus far have been analyzed as if they were shadows of spherically symmetric objects. The formation and analysis of the radiograph of a spherically symmetric object are illustrated schematically in Fig. 123.22 for the case of a hollow spherical shell. Generally, the radial opacity profile $\kappa(r)$ of a hollow spherical shell forms a circularly symmetric intensity distribution $I(x)$, which appears as a characteristically limb-darkened shadow, relative to a uniform backlighter intensity I_{BL}. The optical thickness $\tau(x)$ of a spherically symmetric object is the Abel transform of the opacity profile

$$\tau(x) = \int \kappa\left[r(s)\right] \mathrm{d}s, \tag{2}$$

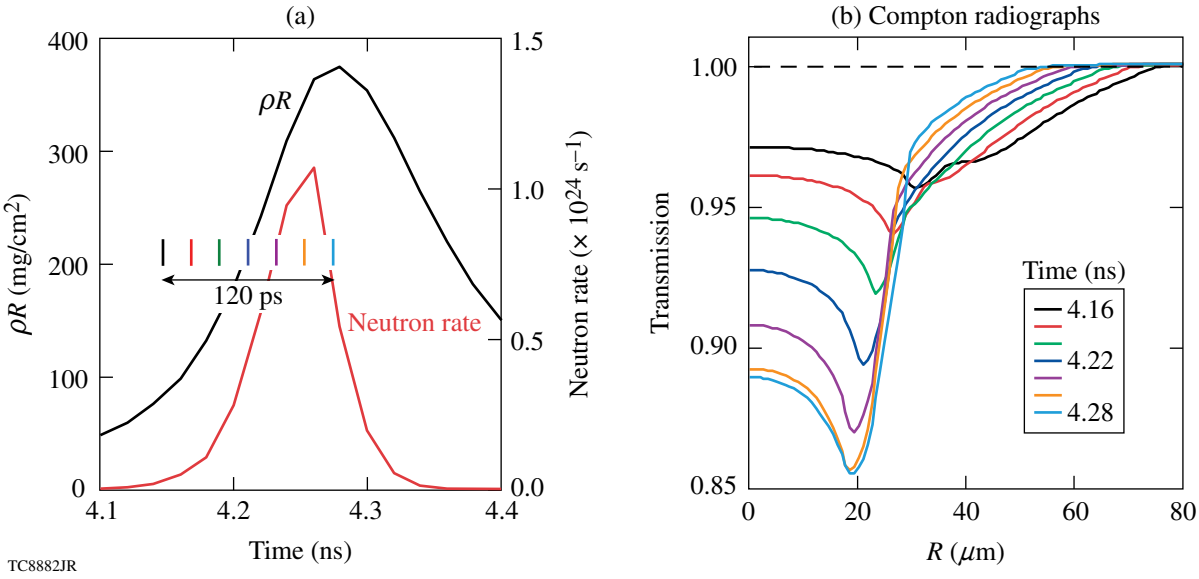

Figure 123.31
A 1-D *LILAC*/Spect3D simulation of a sequence of Compton radiographs has been obtained over the 120 ps leading up to the time of peak compression of shot 55723, which recently attained an areal density of 300 mg/cm^2. The shell areal density and neutron emission rate are plotted in (a) as functions of time. The radiographs are represented in (b) as radial transmission profiles, color-keyed to the time labels in the legend and to time markers in (a). The backlighter photon energy was chosen to be 57 keV. Spatial and temporal resolutions were not taken into account.

where each point on the backlighter ray path s is identified with its distance r from the center of the object. The inverse Abel transform of $\tau(x)$

$$\kappa(r) = -\frac{1}{\pi}\int_r^\infty \frac{\mathrm{d}\tau(x)}{\mathrm{d}x}\frac{\mathrm{d}x}{\sqrt{x^2-r^2}} \tag{3}$$

recovers the spherical opacity profile from the shadow. Limb darkening is the tendency for the radiographic shadow of a uniformly absorbing shell to have a sharp minimum of intensity at a radius equal to the inner radius of the absorbing shell because of the strong peak in $\tau(x)$ at that radius. Obtaining the opacity at a given radius r by Abel inversion requires information from the radiograph only for $x > r$. If, for example, there is an emitting core within a radius r_0, Abel inversion of the radiograph still gives the opacity distribution for $r > r_0$, as long as the shadow is visible for all $x > r_0$. The radial optical thickness can be obtained by evaluating $\int_{r_0}^\infty \kappa(r)\mathrm{d}r$ using Eq. (3) and performing the radial integration analytically to derive a new expression,

$$\int_{r_0}^\infty \kappa(r)\mathrm{d}r = \frac{r_0}{\pi}\int_{r_0}^\infty \frac{\tau(x)}{x\sqrt{x^2-r_0^2}}\mathrm{d}x, \tag{4}$$

which is easier to apply than Eq. (3) if the radial integral is all that is wanted.

A preliminary estimate of the areal density of the imploding target in shot 54395 obtained from a lineout of its radiograph is shown in Fig. 123.32, which illustrates the basic steps of the radiographic analysis. The imploding shell is seen as a crisp shadow near the center of the elliptical backlighter emission spot in (a). The transmission/emission profile is first isolated from this nonuniform backlighter intensity distribution in a highly approximate fashion shown in (b) by fitting an inverted parabola to reconstruct the symmetric rounded top of the backlighter intensity distribution from the portion of the backlighter that is exposed. Emission from the core and from a thin unablated remnant of the original CD shell can be seen peaking above the backlighter intensity in (b). The FF opacity of deuterium at the Al K-shell line energies and a uniform shell temperature estimate of 25 eV from a *LILAC* simulation gives a $\rho^2R \approx 0.097$ g^2/cm^5 for the absorbing shell based on the measured transmission profile and Eq. (4). Assuming that the shell density is uniform, we obtain an areal density of $\rho R \approx 33$ mg/cm^2 within a shell thickness of 110 μm centered at a mean radius of about 140 μm. This areal-density value is consistent with the imploded mass from the *LILAC* simulation of this implosion confined within the shadow radius. Assuming a temperature based on a simulation introduces a weak model dependence into this estimate. The unablated shell mass can be used instead of the shell temperature as a simulation-based parameter.[7] This may be a better choice since, unlike the shell

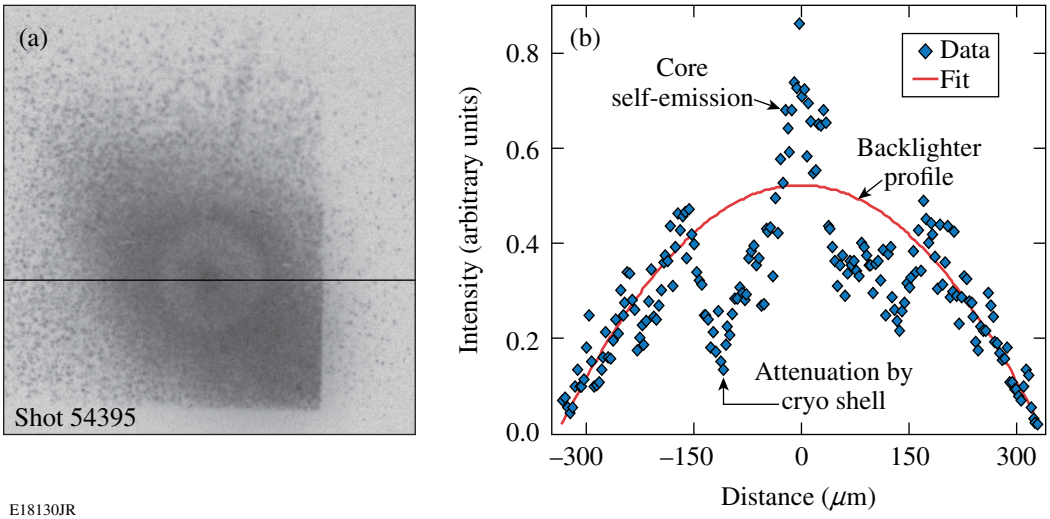

Figure 123.32
A preliminary estimate of the target areal density obtained from a radiograph lineout of shot 54395 illustrates the basic steps of radiograph analysis. The attenuation contribution to the radiograph in (a) is obtained by fitting an inverted parabola model to the backlighter intensity profile shown in (b), where it is not obscured by the imploding shell, and then using this fitted backlighter model profile to infer the backlighter intensity behind the imploding shell. Emission from the core and from a thin unablated remnant of the original CD shell can be seen peaking above the backlighter intensity in (b). The FF opacity of deuterium and a shell-temperature estimate of 25 eV from a *LILAC* simulation give a $\rho^2 R \approx 0.097$ g^2/cm^5 value within the absorbing shell. Assuming that the shell density is uniform, $\rho R \approx 33$ mg/cm^2 can be inferred, which is consistent with the imploded mass from the *LILAC* simulation of this implosion.

temperature, it is nearly constant throughout the approach to peak compression, and it allows one to treat the opacity simply as ρ^2 times a constant determined by the imploded mass value. The flat transmission level within the shell's shadow and the crisp outer boundary defined by the self-emission help to define the shell boundaries, but the extra self-emission at this late time, after the laser pulse has turned off, implies an unablated residue of the original CD shell. Simulation of this implosion verifies that shells must be slightly thinner than in this example to avoid an unablated shell remnant. As has been discussed above, even a trace of residual CD can add significantly to the opacity of the shell. Clearly, this compromises our ability to analyze this imploding shell reliably in terms of the FF opacity of pure D_2.

These areal-density and shell-radius estimates are consistent with a *LILAC* simulation of this implosion roughly 300 ps in advance of peak compression, as can be seen in Fig. 123.33. The time uncertainty indicated by the error bars corresponds to the 80-ps gating time of the x-ray framing camera. These estimates are uncertain due to the small amount of radiographic data sampled by the single lineout and the resulting difficulty in identifying the limits of the shell. These results are sensitive to the fitting model of the backlighter intensity profile.

The radiograph of shot 54395 shown in Fig. 123.32(a) is shown again in Fig. 123.34(b). Another view of the same implosion from another pinhole on the framing camera, approximately 40 ps earlier, is shown in Fig. 123.34(a). The separation of the pinholes on the framing camera creates a parallax effect that changes the position of the imploding target relative to the backlighter spot. The radiograph in (a)

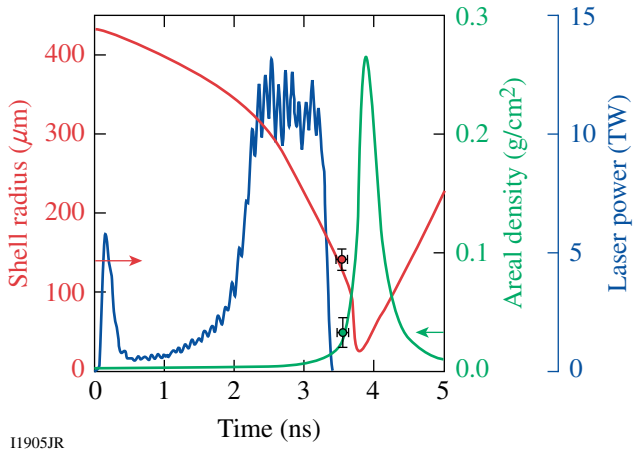

Figure 123.33
The areal density and shell diameter inferred from the preliminary analysis of the first radiograph of shot 54395 are consistent with the *LILAC* simulation of this implosion at a time well before peak compression. Further simulation and analysis of the radiograph indicate that complicating effects of a trace remnant of the original CD shell lends a large uncertainty to the inferred ρR value.

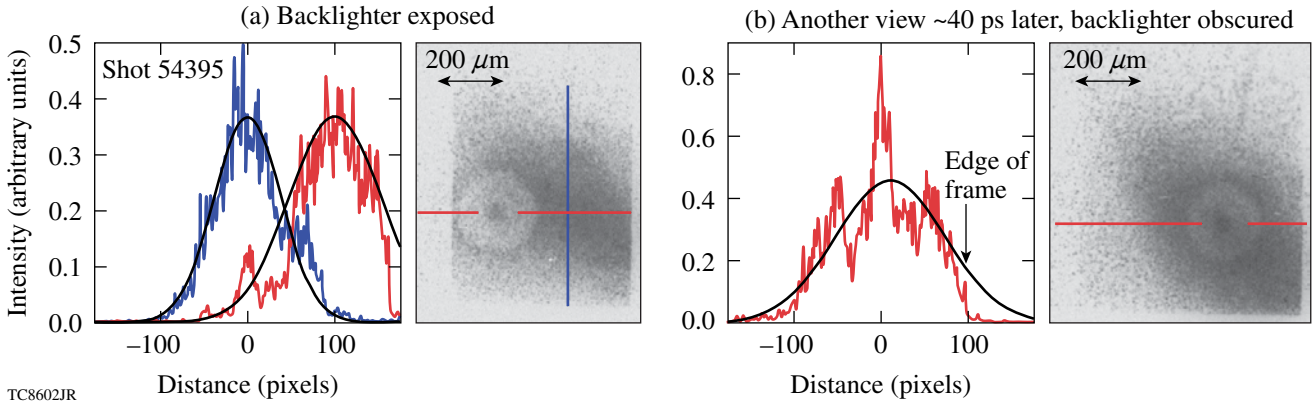

Figure 123.34
Two framing camera views of the same imploding shell, shot 54395, taken at nearly the same time are shown in (a) and (b). Parallax caused by the separation of the pinholes on the framing camera creates images with different target-backlighter orientations. These radiographs are flat fielded with an elliptical Gaussian backlighter distribution model. The superposition of lineouts of the fitted backlighter profile and the radiograph in (a) shows that the elliptical Gaussian profile fits the backlighter profile well. The color of each lineout matches that of the line on the radiograph, indicating the row or column of data represented by the lineout. The good fit of the model distribution to the two orthogonal lineouts in (a) indicates that the attenuation of the center of the backlighter by the imploding target seen in the radiograph in (b) is probably being isolated properly with this model.

shows the center of the backlighter spot exposed, while the radiograph in (b) shows the target well-centered over the backlighter spot, providing a strong absorption signal over the entire target. These radiographs are flat fielded, assuming that the backlighter has an elliptical Gaussian distribution. The plots show lineouts of the radiographs superimposed on the same lineout of the fitted backlighter model. Each lineout is taken along the row or column of data indicated on the radiographs by the line with the matching color. Plot (a) shows that a good fit is obtained over nearly the entire spot, which indicates that the backlighter is being represented properly when this fitting model is applied to the radiograph in (b), where the center of the backlighter distribution is obscured. After the radiograph is flat fielded with the fitted backlighter distribution, the transmission image of the target remains, which is then circularly averaged and Abel inverted to obtain the radial opacity profile of the imploded shell.

The radiograph of shot 54395 in Fig. 123.32(a) has been analyzed using an elliptical Gaussian intensity model fit to the exposed portion of the backlighter spot. The resulting transmission distribution is circularly averaged about the center of the shell shadow and plotted as the blue curve in both frames of Fig. 123.35. The inverse Abel transform given by Eq. (3) is applied to this transmission profile, obtaining a radial opacity profile. This opacity profile is the ρ^2 profile, the density scaling of FF opacity, to within a constant factor that is determined by the total unablated shell mass 34.8 μg obtained from a *LILAC* simulation. The resulting density profile is plotted in red in both frames of Fig. 123.35. Radial transmission profiles were obtained from a *LILAC*/Spect3D simulation at three times covering a 200-ps range centered at the time of the measurement indicated in Fig. 123.33. These are plotted in Fig. 123.35(a), where the measured radial transmission profile is emphasized as a heavy blue curve for easier comparison. The simulated mass density profiles at these three times are plotted in Fig. 123.35(b) along with the measured mass-density profile, plotted in this frame as a heavy red curve. The mass-density distribution is strongly peaked toward the outside of the shell, resulting in an areal density $\rho R = 19$ mg/cm^2, not quite consistent with the preliminary estimate shown in Fig. 123.33. Assuming a 25-eV shell temperature, which is applicable to this time interval, an analysis based on the FF opacity of pure D_2 gives a much higher value of $\rho R = 47$ mg/cm^2, suggesting that the shell is more opaque than a simple understanding of D_2 opacity would lead one to expect.

The simulated and measured transmission profiles in Fig. 123.35 both show transmission factors greater than unity at some radii, which indicates self-emission contributions from the core and from near the outer radius of the shell. The absolute backlighter intensity was not available for the radiographic simulation, so the simulation uniform backlighter intensity value was chosen to have roughly the observed strength of the backlighter relative to the self-emission at the time when the rapidly rising core self-emission and the outer-shell self-emission are comparably intense. The result in Fig. 123.35 is that the exterior self-emissions compare well, while the

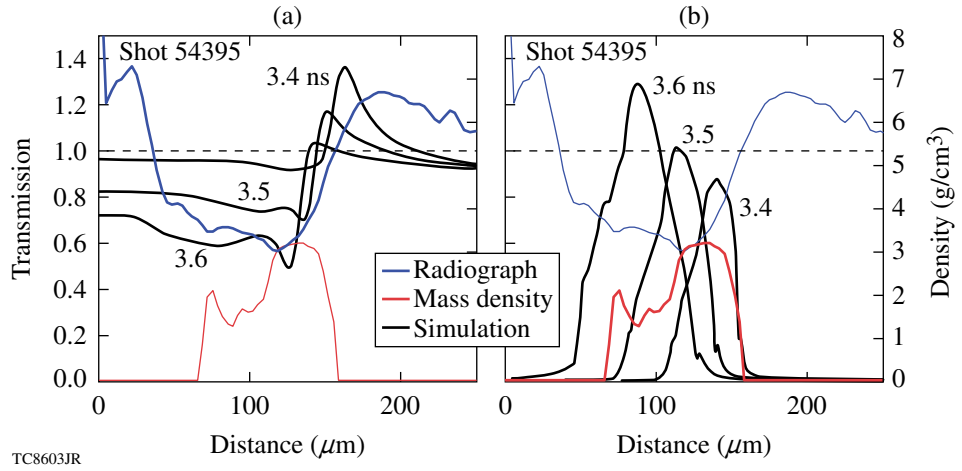

Figure 123.35

The simulation of shot 54395 by *LILAC* shows that a trace of the original CD shell remains unablated. The Spect3D simulated radiographs take this into account and show some resemblance to the measured radiograph between 3.5 and 3.6 ns. The central self-emission is underpredicted at this time, relative to the exterior self-emission, but the amount of unablated CD is known well enough for the simulated and measured exterior self-emissions to match reasonably well. Plots (a) and (b) both show the circularly averaged radial transmission profile and the mass-density profile that is recovered from it by Abel inversion. In (a), the transmission profile (blue) is emphasized and compared with simulated transmission profiles; in (b), the inferred mass-density profile is emphasized (red) and compared with the corresponding simulated mass-density profiles. The inferred density profiles are normalized to the simulated imploded mass. The mass-density profile inferred from analyzing the radiograph in terms of the opacity of D_2 is compromised by the unablated CD, even though it is a small remnant of minimal hydrodynamic importance. The dashed line indicates unit transmission.

simulated core self-emission has not grown to the measured level. It is probably more reliable to match the exterior self-emission since the source is the residual and unablated shell CD, which is predicted to be present in the 1-D simulation, while the strength of the measured shell absorption suggests that shell CD may have mixed into the center of the implosion, which would increase the core self-emission relative to the 1-D prediction by an uncertain factor. The unablated CD remnant is indicated in the simulated mass-density profiles, and its presence accounts for the sharp limb-darkened feature on the simulated transmission profile, which is particularly distinct at the later two times. The generally flat appearance of the shadow in the radiographs in Figs. 123.32(a), 123.34(a), and 123.34(b) suggests that the radial opacity profile is distinctly weighted toward the exterior, which is borne out in the more thorough analysis summarized in Fig. 123.35. The presence of unablated CD compromises the analysis of the radiograph in terms of the opacity of pure D_2, even if the amount of CD involved is of minor hydrodynamic significance. In another shot, a slight reduction in the initial CD thickness produces an imploded shell where the CD is predicted to be completely ablated away, providing a case that is potentially much better suited for this kind of analysis.

This analysis of the radiograph of shot 54395 has been repeated for shot 55133 and is shown in Fig. 123.36. The polymer shell of this target was 9.6 μm thick, initially, which was sufficiently reduced from the 10.1-μm shell thickness of shot 54395 that no polymer remains in the unablated shell in the *LILAC* simulation. As expected, the radiograph, included in Fig. 123.36 as an inset, shows no apparent self-emission at its outer edge, indicating that there is no residual polymer. Plots (a) and (b) both show the same circularly averaged radial transmission profile and the mass-density profile that was recovered from it by Abel inversion. The inferred density profile, normalized to the simulated imploded mass of 33.5 μg, has an areal density of 20 mg/cm^2, much lower than the value based on the opacity, 56 g/cm^2. In this figure, the simulated density profiles were time averaged over the 80-ps time gate of the framing camera.

The inferred mass-density profile is flatter and broader than any of the time-averaged simulated profiles. Consistent with this, the measured radiographic transmission profile is broader than the simulated radiographs at any time. Since the measured radiograph shows no sign of self-emission other than from the core, the simulated radiographs were calculated without self-emission to obtain a pure transmission signal. Consequently, the simulated and measured radiographs cannot be compared within the emitting core radius. This does not affect the inferred density profile outside the emitting core. The simulated and measured radiographs and density profiles bear

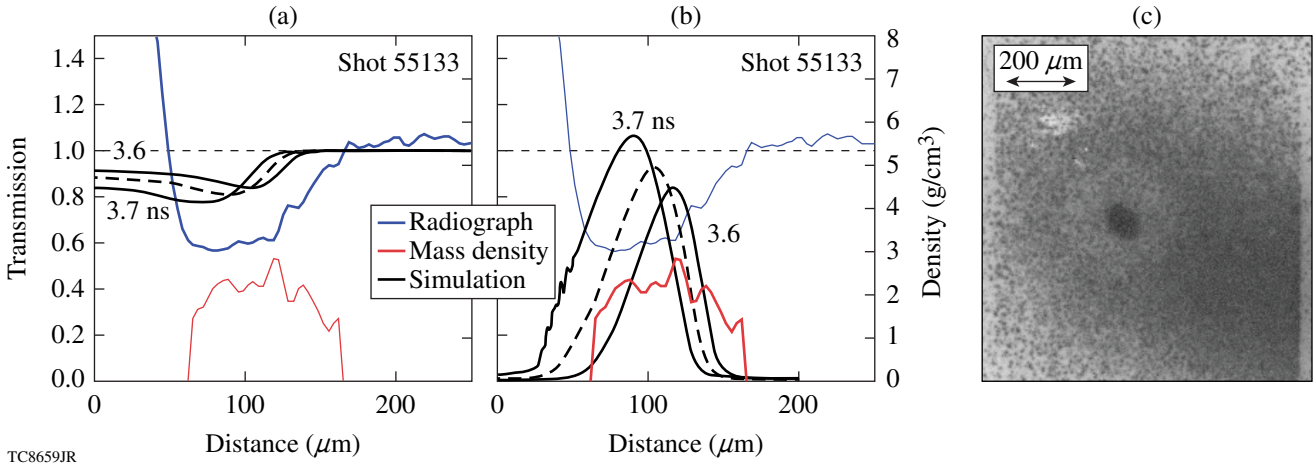

Figure 123.36
The analysis of the radiograph of shot 54395 illustrated in Fig. 123.35 is repeated here for a radiograph of shot 55133, shown in (c). This polymer shell is 9.6 μm thick, less than 10.1 μm for shot 54395. As a result, all of the polymer is expected to be ablated away, and no self-emission or absorption from unablated polymer is either expected or seen. The mass-density profile (red curve) in (b) that has been inferred from the transmission profile in (a) matches the position of the simulated shell most closely at 3.6 ns. The plotted simulated density profiles have been averaged over the 80-ps time gate of the framing camera. The areal density from the inferred mass distribution, normalized to the simulated imploded mass of 33.5 μg, is 20 mg/cm^2, much lower than the value based on the opacity, 56 mg/cm^2. The observed attenuation at this time is significantly greater than expected, as if an excess opacity were distributed uniformly over the shell.

a closer qualitative resemblance in this case than in the case of shot 45395, primarily because there is no localized external self-emission, but the measured radiographic attenuation is still greater than expected.

This unaccounted absorption remains under investigation. Small-scale mix of the shell polymer into the D_2 shell is a possibility, although an amount of carbon sufficient to diminish the transmission should be visible as self-emission at the outer surface of the shell, still warm from the ablation phase of the implosion. The D_2 opacity model must be examined. Additional BF opacity could add significantly to the opacity if the D ions are not as completely stripped by continuum lowering as the model indicates.[19]

Conclusions

Radiography of cryogenic implosions with OMEGA EP–driven backlighting is being developed on OMEGA. Analysis of the first OMEGA/OMEGA EP FF radiographs has provided useful measurements at times well in advance of peak compression. Simulated radiographs based on a multidimensional cryogenic implosion demonstrate that FF radiography at peak compression is feasible with the demonstrated backlighter intensity. Compton radiography with hard x-ray point backlighters, an alternative to radiography with soft area backlighters, has been demonstrated on OMEGA with CH implosions and is also under development for cryogenic implosion imaging on OMEGA. There is a balance of advantages between FF and Compton radiography. Compton radiographs, with simpler backlighter attenuation physics and lower background from self-emission, are easier to analyze. Simulated Compton radiographs show measurable contrast that is interpreted with simple attenuation physics with little dependence on the backlight spectrum or the target material. The strong material dependence of FF opacity can compromise the soft radiograph of a cryo shell, even if only a trace of polymer shell material mixes into the imploded ice. While the very weak material dependence of Compton scattering makes radiography of the ice shell possible in the presence of hydrodynamically irrelevant contaminants, the stronger material sensitivity of FF radiography could be useful for detecting significant contamination or mix. Not only is the radiograph contrast much stronger in FF radiography, as compared with the marginally detectable contrast in Compton radiography, but the contrast can be optimized for a particular stage in the compression history by changing the backlighter material, while in Compton radiography almost nothing can be done to improve or adjust the contrast.

With either method, backlighter sources driven by OMEGA EP will provide useful images of cryogenic shells imploded on OMEGA. The images obtained from the radiography of cryogenic implosions will be crucial for demonstrating the continuing success of cryogenic implosion campaigns by supplementing the data currently obtained. The preliminary results presented here show similarities between the simulated

implosion performance and radiography well in advance of peak compression. These results are valuable and encouraging in planning for future measurements that will be extended to the final phases of the implosion.

ACKNOWLEDGMENT

This work was supported by the U.S. Department of Energy Office (DOE) of Inertial Confinement Fusion under Cooperative Agreement No. DE-FC52-08NA28302, the University of Rochester, and the New York State Energy Research and Development Authority. The support of DOE does not constitute an endorsement by DOE of the views expressed in this article.

REFERENCES

1. T. R. Boehly, D. L. Brown, R. S. Craxton, R. L. Keck, J. P. Knauer, J. H. Kelly, T. J. Kessler, S. A. Kumpan, S. J. Loucks, S. A. Letzring, F. J. Marshall, R. L. McCrory, S. F. B. Morse, W. Seka, J. M. Soures, and C. P. Verdon, Opt. Commun. **133**, 495 (1997).

2. L. J. Waxer, D. N. Maywar, J. H. Kelly, T. J. Kessler, B. E. Kruschwitz, S. J. Loucks, R. L. McCrory, D. D. Meyerhofer, S. F. B. Morse, C. Stoeckl, and J. D. Zuegel, Opt. Photonics News **16**, 30 (2005).

3. V. N. Goncharov, T. C. Sangster, T. R. Boehly, S. X. Hu, I. V. Igumenshchev, F. J. Marshall, R. L. McCrory, D. D. Meyerhofer, P. B. Radha, W. Seka, S. Skupsky, C. Stoeckl, D. T. Casey, J. A. Frenje, and R. D. Petrasso, Phys. Rev. Lett. **104**, 165001 (2010); T. C. Sangster, V. N. Goncharov, R. Betti, T. R. Boehly, D. T. Casey, T. J. B. Collins, R. S. Craxton, J. A. Delettrez, D. H. Edgell, R. Epstein, K. A. Fletcher, J. A. Frenje, V. Yu. Glebov, D. R. Harding, S. X. Hu, I. V. Igumenshchev, J. P. Knauer, S. J. Loucks, C. K. Li, J. A. Marozas, F. J. Marshall, R. L. McCrory, P. W. McKenty, D. D. Meyerhofer, P. M. Nilson, S. P. Padalino, R. D. Petrasso, P. B. Radha, S. P. Regan, F. H. Seguin, W. Seka, R. W. Short, D. Shvarts, S. Skupsky, V. A. Smalyuk, J. M. Soures, C. Stoeckl, W. Theobald, and B. Yaakobi, Phys. Plasmas **17**, 056312 (2010).

4. C. D. Zhou and R. Betti, Phys. Plasmas **14**, 072703 (2007).

5. E. I. Moses, J. Phys., Conf. Ser. **112**, 012003 (2008).

6. R. Epstein, V. A. Smalyuk, F. J. Marshall, J. Delettrez, V. N. Goncharov, P. W. McKenty, D. D. Meyerhofer, P. B. Radha, S. P. Regan, T. C. Sangster, and W. Theobald, Bull. Am. Phys. Soc. **54**, 306 (2009).

7. F. J. Marshall, P. W. McKenty, J. A. Delettrez, R. Epstein, J. P. Knauer, V. A. Smalyuk, J. A. Frenje, C. K. Li, R. D. Petrasso, F. H. Séguin, and R. C. Mancini, Phys. Rev. Lett. **102**, 185004 (2009).

8. R. Tommasini *et al.*, Rev. Sci. Instrum. **79**, 10E901 (2008).

9. *LLE Review Quarterly Report* **120**, 239, Laboratory for Laser Energetics, University of Rochester, Rochester, NY, LLE Document No. DOE/NA/28302-910 (2009).

10. D. K. Bradley *et al.*, Rev. Sci. Instrum. **66**, 716 (1995).

11. S. Regan (Laboratory for Laser Energetics) and R. Tommasini (Lawrence Livermore National Laboratory), private communication (2009).

12. S. Chandrasekhar, *Plasma Physics* (University of Chicago Press, Chicago, 1960).

13. R. N. Bracewell, *The Fourier Transform and Its Applications*, 3rd ed. (McGraw-Hill, Boston, 2000).

14. E. Sergrè, *Nuclei and Particles: An Introduction to Nuclear and Subnuclear Physics* (W. A. Benjamin, New York, 1965).

15. J. Castor, *Radiation Hydrodynamics* (Cambridge University Press, Cambridge, England, 2004), pp. 291–293.

16. J. D. Lindl, Phys. Plasmas **2**, 3933 (1995).

17. J. Delettrez, R. Epstein, M. C. Richardson, P. A. Jaanimagi, and B. L. Henke, Phys. Rev. A **36**, 3926 (1987).

18. P. B. Radha, V. N. Goncharov, T. J. B. Collins, J. A. Delettrez, Y. Elbaz, V. Yu. Glebov, R. L. Keck, D. E. Keller, J. P. Knauer, J. A. Marozas, F. J. Marshall, P. W. McKenty, D. D. Meyerhofer, S. P. Regan, T. C. Sangster, D. Shvarts, S. Skupsky, Y. Srebro, R. P. J. Town, and C. Stoeckl, Phys. Plasmas **12**, 032702 (2005).

19. J. J. MacFarlane *et al.*, High Energy Density Phys. **3**, 181 (2006).

20. T. C. Sangster, V. N. Goncharov, P. B. Radha, V. A. Smalyuk, R. Betti, R. S. Craxton, J. A. Delettrez, D. H. Edgell, V. Yu. Glebov, D. R. Harding, D. Jacobs-Perkins, J. P. Knauer, F. J. Marshall, R. L. McCrory, P. W. McKenty, D. D. Meyerhofer, S. P. Regan, W. Seka, R. W. Short, S. Skupsky, J. M. Soures, C. Stoeckl, B. Yaakobi, D. Shvarts, J. A. Frenje, C. K. Li, R. D. Petrasso, and F. H. Séguin, Phys. Rev. Lett. **100**, 185006 (2008).

21. W. Theobald, C. Stoeckl, P. A. Jaanimagi, P. M. Nilson, M. Storm, D. D. Meyerhofer, T. C. Sangster, D. Hey, A. J. MacKinnon, H.-S. Park, P. K. Patel, R. Shephard, R. A. Snavely, M. H. Key, J. A. King, B. Zhang, R. B. Stephens, K. U. Akli, K. Highbarger, R. L. Daskalova, L. Van Woerkom, R. R. Freeman, J. S. Green, G. Gregori, K. Lancaster, and P. A. Norreys, Rev. Sci. Instrum. **80**, 083501 (2009).